# Phonon modes and electron–phonon coupling at the FeSe/SrTiO$_3$ interface

https://doi.org/10.1038/s41586-024-08118-0

Received: 18 January 2024

Accepted: 25 September 2024

Hongbin Yang[1], Yinong Zhou[2], Guangyao Miao[3], Ján Rusz[4], Xingxu Yan[1], Francisco Guzman[1], Xiaofeng Xu[3], Xianghan Xu[5], Toshihiro Aoki[6], Paul Zeiger[4], Xuetao Zhu[3], Weihua Wang[3], Jiandong Guo[3], Ruqian Wu[2] & Xiaoqing Pan[1,6] ✉

The remarkable increase in superconducting transition temperature ($T_c$) observed at the interface of one-unit-cell FeSe films on SrTiO$_3$ substrates (1 uc FeSe/STO)[1] has attracted considerable research into the interface effects[2–6]. Although this high $T_c$ is thought to be associated with electron–phonon coupling (EPC)[2], the microscopic coupling mechanism and its role in the superconductivity remain elusive. Here we use momentum-selective high-resolution electron energy loss spectroscopy to atomically resolve the phonons at the FeSe/STO interface. We uncover new optical phonon modes, coupling strongly with electrons, in the energy range of 75–99 meV. These modes are characterized by out-of-plane vibrations of oxygen atoms in the interfacial double-TiO$_x$ layer and the apical oxygens in STO. Our results also demonstrate that the EPC strength and superconducting gap of 1 uc FeSe/STO are closely related to the interlayer spacing between FeSe and the TiO$_x$ terminated STO. These findings shed light on the microscopic origin of the interfacial EPC and provide insights into achieving large and consistent $T_c$ enhancement in FeSe/STO and potentially other superconducting systems.

Extensive studies on the electronic structure of 1 unit cell (uc) FeSe/STO have shown that charge transfer from oxide substrates is essential for the enhanced superconducting transition temperature ($T_c$)[7–9]. Although electron doping of FeSe without oxide substrates raises its $T_c$ to around 40 K (refs. 10–12), 1 uc FeSe/STO shows even higher $T_c$[13,14]. The enhanced pairing is also evidenced by the significantly higher gap-closing temperature up to 80 K and the large superconducting gap of nearly 20 meV, as observed through angle-resolved photoemission spectroscopy (ARPES)[15–17] and scanning tunnelling microscopy and spectroscopy (STM–STS)[1,8,18]. A critical factor contributing to the exceptional $T_c$ enhancement is the coupling with interfacial bosonic modes, as indicated by the replica electron bands in ARPES[2,5,19–21]. Oxygen optical phonons in STO are often considered responsible for the replica bands and the resulting EPC. Additionally, Fuchs–Kliewer phonons[22], observed in reflection electron energy loss spectroscopy (EELS) studies[23,24], have also been linked to the EPC due to the long-ranged electrical field.

Atomic-resolution imaging by scanning transmission electron microscopy (STEM) have observed an interfacial double-TiO$_x$ layer[25–27], revealing that the STO substrate is not in direct contact with the 1 uc FeSe film. The substantial spatial separation between the FeSe electrons and the STO lattice contrasts with most bulk superconductors, raising questions on the microscopic mechanism of the cross-interface coupling. The connection between the structure, phonons, and EPC at the FeSe/STO interface, remains unclear.

Here, we use monochromated EELS in an aberration-corrected STEM[28] to directly image phonons across the FeSe/STO interface with atomic column sensitivity[29–31]. Whereas this technique has recently been applied to study the FeSe/STO interface[6], the accompanying large momentum integration[32] poses challenges in understanding phonons at a complex interface. To identify the phonon modes with significant contribution to EPC, here we use a newly developed technique[33] to separately measure the in-plane and out-of-plane vibrations. Out-of-plane vibrations of oxygen atoms in the interfacial TiO$_x$ layers and the adjacent STO substrate are directly imaged at atomic resolution using momentum-selective EELS, which we further analysed using density-functional theory (DFT) and frequency-resolved frozen phonon multislice (FRFPMS) simulations. We also investigated 1 uc FeSe/STO samples under varying annealing conditions and demonstrated that interlayer spacing is a key parameter for the $T_c$ enhancement.

We grew FeSe films on STO using molecular beam epitaxy and measured the superconducting gap of 1 uc FeSe/STO samples by STM–STS at 5 K. Figure 1a shows a d$I$/d$V$ curve of the sample postannealed in ultrahigh vacuum (UHV) at 500 °C for 2 h, revealing a superconducting gap of approximately 18 meV, which confirms the enhanced superconductivity.

Following the STM–STS measurements, we deposit a Te protection layer on top of the FeSe film to prevent oxidation before subsequent STEM–EELS study. Cross-section TEM specimens are prepared using a standard lift-out process. High-angle annular dark-field (HAADF) STEM imaging reveals continuous FeSe films with good uniformity, even at 1 uc thick (Extended Data Fig. 1). The atomic-resolution HAADF image in Fig. 1b shows an extra atomic layer of TiO$_x$ between the 1 uc FeSe film and the TiO$_2$ terminated STO substrate, which we refer as the Ti–O layer 0 in this study. This TiO$_x$ layer, characteristic of a

---

[1] Department of Materials Science and Engineering, University of California, Irvine, CA, USA. [2] Department of Physics and Astronomy, University of California, Irvine, CA, USA. [3] Beijing National Laboratory for Condensed Matter Physics and Institute of Physics, Chinese Academy of Sciences, Beijing, China. [4] Department of Physics and Astronomy, Uppsala University, Uppsala, Sweden. [5] Department of Chemistry, Princeton University, Princeton, NJ, USA. [6] Irvine Materials Research Institute (IMRI), University of California, Irvine, CA, USA. ✉e-mail: xiaoqinp@uci.edu

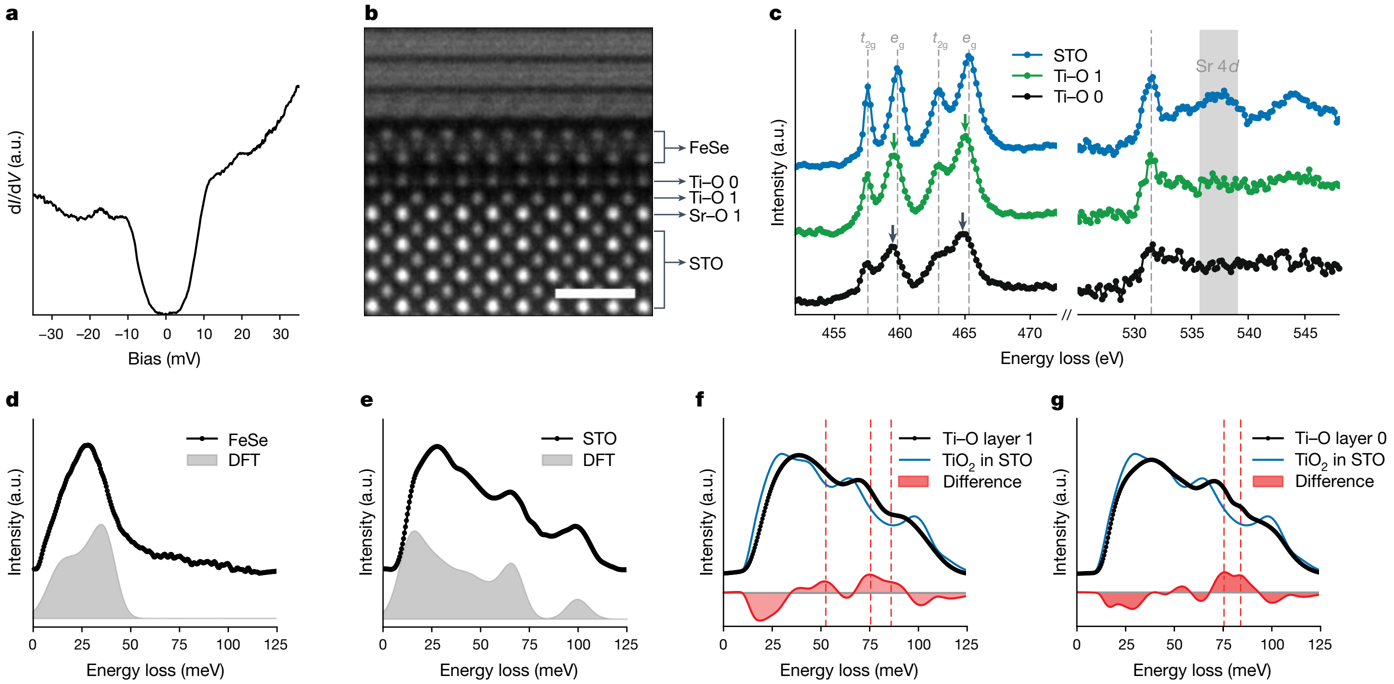

**Fig. 1 | Interface structure and vibrational spectra of superconducting 1 uc FeSe/STO. a**, A d*I*/d*V* curve of a 1 uc FeSe/STO sample measured at 5 K. **b**, HAADF-STEM image of a Te capped 1 uc FeSe/STO sample along the [010] zone axis of STO. **c**, Core-loss EELS of Ti-$L_{2,3}$ edges and O-K edges measured from Ti–O layer 0, 1 and the STO substrate. **d**,**e**, Vibrational EELS of FeSe (**d**) and STO (**e**) compared with DFT phonon density of states (grey shading). **f**,**g**, Vibrational EELS of Ti–O layer 1 (**f**) and 0 (**g**), with the TiO$_2$ layers in STO (blue curves) shown for comparison. The red shading highlights the difference between interfacial and bulk vibrational spectra, with interface phonons indicated by the vertical dashed lines. Scale bar, 10 Å.

reconstructed STO surface[34–36], has been consistently observed at FeSe/STO interfaces in previous STEM studies[25–27]. Despite evidence for potential $(\sqrt{5}\times\sqrt{5})$R26.6° and $(\sqrt{13}\times\sqrt{13})$R33.7° reconstructions[2,37,38], the exact structure at the FeSe/STO interfaces is not fully resolved.

To better understand the interfacial structure and bonding, we perform high-resolution core-loss EELS. As shown in Fig. 1c, the $e_g$ peak of T–$L_{2,3}$ edge redshifts by 0.3 eV going from the STO substrate to the double-TiO$_x$ layers. The reduced crystal-field splitting is probably caused by the TiO$_5$ truncated octahedrons from the STO surface reconstruction[36], suggesting the presence of Ti$^{3+}$ at the interface. The O–K edges show similar onset energy but differ at the second peak near 538 eV, which is due to the absence of a Sr 4*d* state in the double-TiO$_x$ layers. Taken together, we believe Ti–O layer 0 consists of a periodic network of TiO$_5$ truncated octahedrons featuring Ti–O bonding with the Ti–O layer 1 (Supplementary Information, 'Interface structure analysis').

Next, we investigate the phonons across the FeSe/STO interface. EELS in the phonon energy range is acquired from electrons scattered in the dark-field regions of the diffraction plane to minimize the influence of delocalized phonon polariton signal[39,40] (Methods). Figure 1d,e shows that the measured phonons of the FeSe film and the STO substrate agree well with the phonon density of states from DFT calculations. At the interface, the Ti–O layer 1 shows a vibrational spectrum that differs from the TiO$_2$ layers in STO (Fig. 1f). By comparing the two EEL spectra, we identify new vibrational modes specific to the interface (interface phonons) near 53 meV and between 75 and 88 meV (red shading). A more pronounced change in vibrational spectrum occurs at Ti–O layer 0, where the interface modes near 76 and 84 meV are more distinct (Fig. 1g).

To gain deeper insight into the phonons at FeSe/STO interface, we further refine our dark-field EELS experiment by introducing selectivity in the momentum transfer (**q**) direction. We deliberately position the EELS entrance aperture either parallel or perpendicular to the interface plane (Fig. 2a,b and Extended Data Fig. 2). Thanks to **q**·**e** terms in the differential scattering cross-section, this gives higher weight to modes with atomic displacements parallel to **q** (ref. 41), thus allowing selective probing of in-plane (IP) or out-of-plane (OP) vibrations, respectively (Methods).

Using this refined approach, we then explore the atomic column-resolved EELS from out-of-plane and in-plane measurements. Figure 2c–e highlight the vibrational anisotropy of the interface. For instance, Fig. 2c presents the EELS of oxygen columns in Sr–O layer 1, where the 100 meV optical phonon peak is prominent in out-of-plane EELS but is rather weak in the in-plane EELS (filled and open arrows). Conversely, the optical phonon peak of oxygen in the Ti–O layer 1 is stronger in the in-plane EELS, as shown in Fig. 2d. Such vibrational anisotropy can be attributed to the preference of oxygen vibration along the Ti–O bond direction near 100 meV, where longitudinal optical phonons predominate. In Ti–O layer 0, despite the phonon peaks being less pronounced due to lowered symmetry, a stronger 93 meV optical phonon peak is still observed in the out-of-plane EELS. Noticeable vibrational anisotropy was also identified in our DFT simulations (Supplementary Information). Furthermore, new oxygen vibration peaks near 85 and 76 meV are shown in Fig. 2d,e, which are absent in the oxygen columns of STO (Extended Data Fig. 3).

Leveraging the high spatial and energy resolutions, along with the selectivity in the **q**-transfer direction, we conduct atomic-resolution dark-field EELS mapping for the interface, resulting in two sets of phonon spectral images (Fig. 2f–i). The energy-filtered images are obtained by integrating within the labelled energy window. Images in Fig. 2f,g are formed by phonons of the STO substrate and FeSe film. The substrate region shows the atomic columns of Sr, Ti+O and O in the spectral image at 15, 40–70 and 100 meV, respectively. Phonons in FeSe are below 50 meV, thus appear primarily in the 15 meV image along with the Sr columns in STO. The medium energy optical phonons (40–70 meV) involve rotations of the TiO$_6$ octahedra (Extended Data Fig. 4a,b), whereas the high-energy ones are primarily O stretching vibrations. In the 99 meV images, we observe the apical and equatorial O columns in the out-of-plane and in-plane images, located within

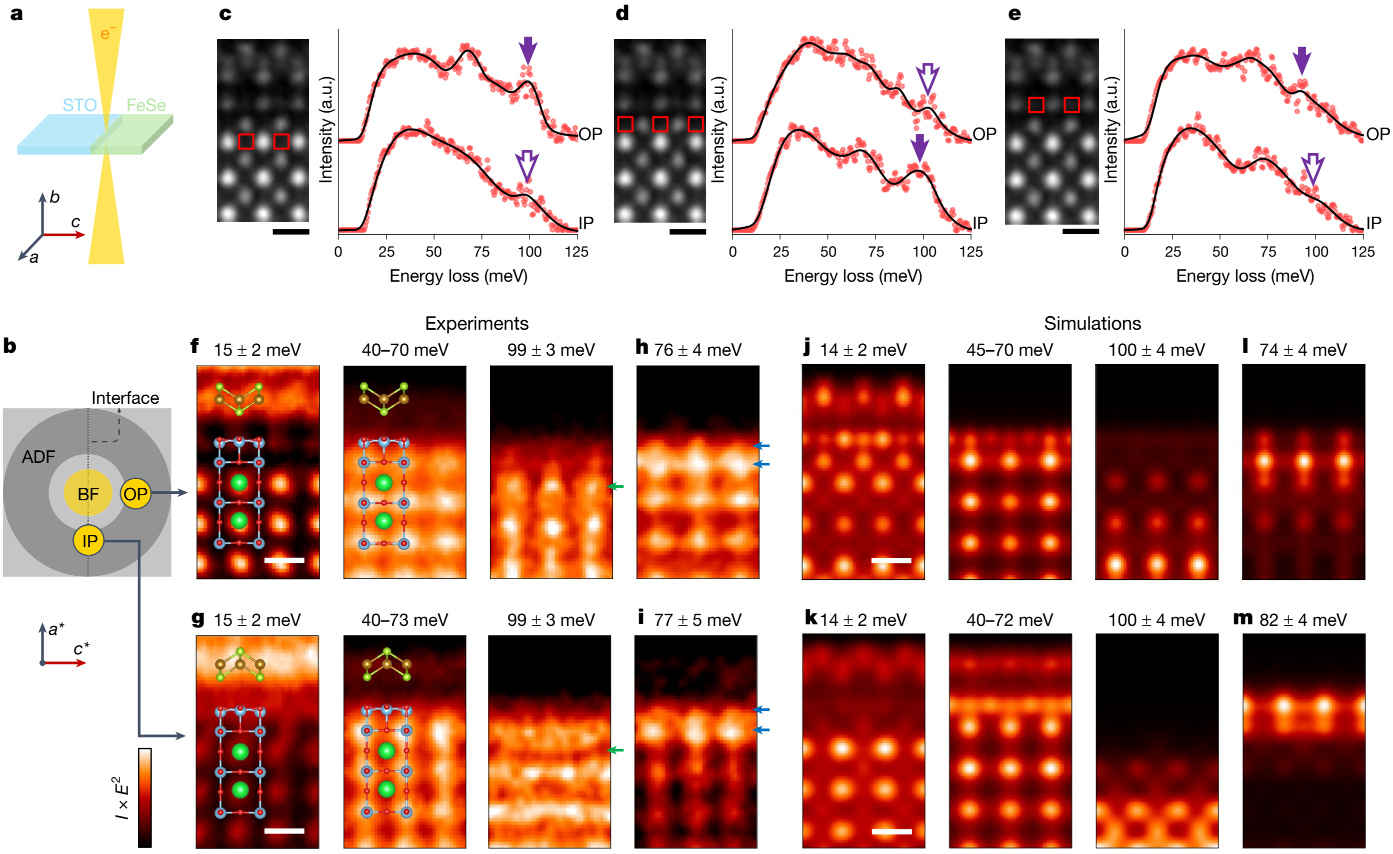

**Fig. 2 | Atomically resolved phonon spectroscopy and imaging. a**,**b**, Schematic of the STEM–EELS experiment (**a**) and the diffraction pattern (**b**) with EELS entrance aperture locations for out-of-plane (OP) and in-plane (IP) acquisitions. The direction of the FeSe/STO interface in real space is indicated by the vertical dashed line. **c**–**e**, Atomic column-resolved EELS of the interfacial layers from out-of-plane and in-plane acquisitions: O columns in Sr–O layer 1 (**c**), O columns in Ti–O layer 1 (**d**) and 'O' columns in Ti–O layer 0 (**e**). The blacklines are spline fit of background subtracted EELS data. The real-space acquisition locations are marked with the red rectangles in the HAADF image on the left. The filled and empty arrows indicate strong and weak optical phonon peaks, respectively. **f**,**g**, Bulk phonons from out-of-plane (**f**) and in-plane acquisition (**g**). **h**,**i**, Interface phonons from out-of-plane (**h**) and in-plane acquisition (**i**). The position of the double-$TiO_x$ layers and Sr–O layer 1 are indicated by the blue and green arrows. **j**–**m**, FRFPMS simulation of the phonon maps corresponding to **f**–**i**. ADF, annular dark field; BF, bright field disk. Scale bars, 4 Å.

the Sr–O layers and Ti–O layers, respectively. As mentioned above, this energy corresponds to the longitudinal opticals phonons of STO, which involve O stretching vibrations along the Ti–O bonds. These observations are corroborated by our FRFPMS simulations[42] shown in Fig. 2j,k. In our FRFPMS simulations, we used DFT-calculated vibrational properties as input and considered the EELS collection aperture positions (Methods).

The atomically resolved phonon maps clearly show the interface vibrations. The double-$TiO_x$ layers exhibit stronger vibrational signal near 53, 76 and 84 meV, with the primary interface phonons observed near 76 meV in Fig. 2h,i, consistent with the simulated phonon maps in Fig. 2l,m. Detailed analyses suggest that the 76 and 84 meV interface modes (Extended Data Fig. 4) originate from different oxygen sites in the double-$TiO_x$ layers. As shown in Fig. 2h, the 76 meV out-of-plane image highlights the 'oxygen' columns in Ti–O layer 0, distinguishing it from other vibrational modes. Conversely, the out-of-plane image at 84 meV shows less involvement of oxygen in Ti–O layer 0, with stronger contribution from oxygen in Ti–O layer 1, probably due to its out-of-plane Ti–O bonding (Extended Data Fig. 3). The energy and atomic columns of these interface vibrations can also be traced back to the EEL spectral features in Figs. 1f,g and 2d,e. The extra details provide the atomic-scale origin of the interface vibrations for studying other physical properties, such as EPC and superconductivity. Slight discrepancies between experiments and simulations in terms of energy and image contrast are noted, potentially due to the difference in the structure of Ti–O layer 0 and limited STO thickness in our DFT calculations.

To study the role of the extra Ti–O layer in the $T_c$ enhancement, we perform first-principles calculations on the FeSe/STO with the $TiO_x$ interface layer. Given the complexities of its structures, here we focus on the $Ti_2O_2$ interlayer structures with the lowest formation energy (Supplementary Fig. 6). The phonon dispersions of FeSe/$Ti_2O_2$/STO (1 uc) are plotted in Fig. 3a, along with the calculated phonon linewidths for the two modes with significant contribution to the EPC. The phonon linewidth peaks strongly around $\mathbf{q} = 0$, indicating the strong forward scattering[2,43,44]. Both the high-energy mode at 78.0 meV and the low-energy mode at 65.7 meV involve out-of-plane vibrations of oxygen atoms at the interface (Extended Data Fig. 5). Furthermore, we directly calculate the Eliashberg spectral function $\alpha^2F(\omega)$ and find $\lambda = 0.57$ for the FeSe/$Ti_2O_2$/STO system, as shown in Fig. 3b (Supplementary Information, 'EPC analysis').

Phonons of a FeSe/$Ti_2O_2$/STO model with 3 uc of STO are also calculated to better compare with experiments. The high- and low-energy phonons in Fig. 3a are shifted to 91 and 75 meV in the 3 uc model, respectively, as shown in Fig. 3c. The 91 meV high-energy mode originates from the O atoms in the Sr–O layer 1. This mode corresponds well with the apical oxygen vibrations in the 99 meV out-of-plane phonon map, which has the same origin as the 100 meV longitudinal optical phonons of STO. The 75 meV low-energy phonon primarily originates from the out-of-plane vibrations of O atoms in the Ti–O layer 1. This mode is

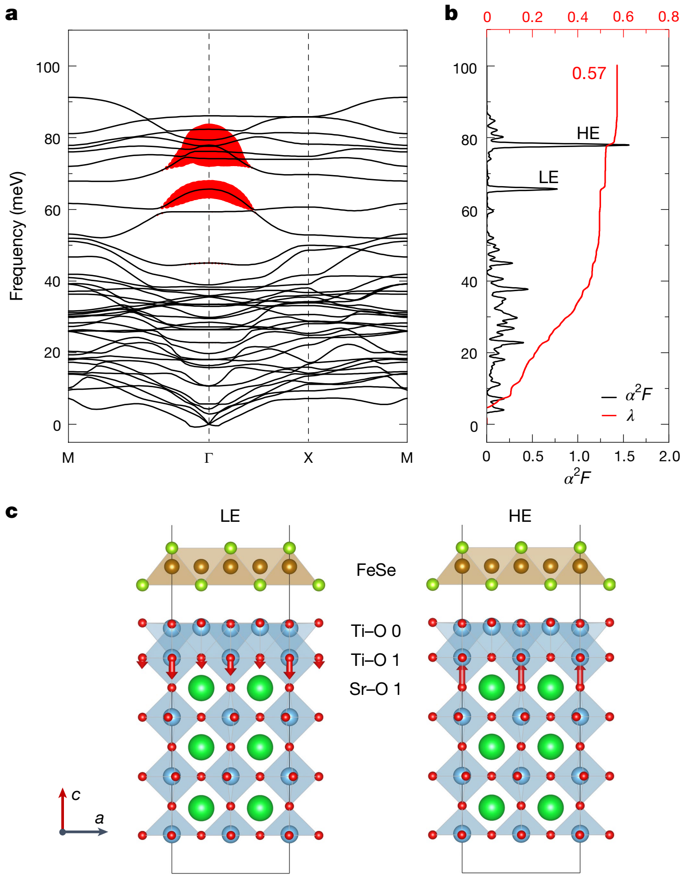

**Fig. 3 | EPC from DFT. a**, Phonon dispersions of FeSe/Ti$_2$O$_2$/STO (1 uc). The phonon linewidths of the low-energy (LE) and high-energy (HE) modes at 65.7 and 78.0 meV are denoted by the size of red dots. **b**, The Eliashberg spectral function $\alpha^2F(\omega)$ and cumulative frequency-dependent EPC strength $\lambda(\omega)$, represented by the black and red curves, respectively. **c**, The structure model of FeSe/Ti$_2$O$_2$/STO (3 uc). The atomic displacement patterns of the LE and HE modes at $\mathbf{q} = 0$ are labelled by red arrows.

probably associated with the new out-of-plane vibrations of oxygen in Ti–O layer 1, which are detected in EELS near 76 and 84 meV. New phonon modes with strong contribution to EPC are enabled by the extra TiO$_x$ layer at the interface, as it introduces out-of-plane Ti–O bonding between the double-TiO$_x$ layers.

Furthermore, our DFT calculations demonstrate the interfacial TiO$_x$ can introduce additional bands crossing the Fermi level, with charge density distributed around the Ti–O layer 0 and 1, Sr–O layer 1, as well as the FeSe monolayer (Extended Data Fig. 6). Because of these bands, the electrons and out-of-plane oxygen phonons coexist at the double-TiO$_x$ layers and the first unit cell of STO. The spatial overlap between the electron and phonon wave functions makes such a region crucial for the interfacial EPC.

It is important to note that the double-TiO$_x$ interface is not the sole type of atomic structure observed in the FeSe/STO samples. Figure 4a shows a different type of interface that features an extra layer of atoms between the FeSe and the double-TiO$_x$ interface. The extra layer possibly consists of Se atoms according to core-loss EELS[45], which enlarges the distance between the first unit cell of FeSe and the STO substrate. For the double-TiO$_x$ type interface, the interlayer spacing, $d_{\text{Fe-Ti}}$, defined as the distance between Fe plane in the 1 uc FeSe and Ti–O layer 0, measures approximately 4.3 Å. For the Se/TiO$_x$ interface, $d_{\text{Fe-Ti}}$ is as large as 6.5 Å. The phonon intensities across the two types of interface are shown in the right panels of Fig. 4a,b. The intensities of both 75 and 99 meV phonons decrease when approaching the 1 uc FeSe. In the case of the large $d_{\text{Fe-Ti}}$ interface, the 1 uc FeSe is further separated from the STO substrate, which reduces the spatial overlap between the Fe electrons and the strong-coupling phonons.

HAADF imaging of a series of FeSe/STO samples reveals that the local interface structures are characterized by either a large $d_{\text{Fe-Ti}}$ of more than 6 Å or a small $d_{\text{Fe-Ti}}$ of nearly 4.3 Å, as summarized in Fig. 4c. In thick (10 uc) FeSe films grown on STO substrate, only large $d_{\text{Fe-Ti}}$ interfaces are observed. For the annealed 1 uc FeSe/STO samples, both small and large $d_{\text{Fe-Ti}}$ interfaces coexist. Specifically, the small $d_{\text{Fe-Ti}}$, double-TiO$_x$ structure predominates in the 500 °C annealed 1 uc FeSe/STO sample, as shown in Figs. 1b and 4b. Whereas in the as-grown (non-superconducting) and lower temperature (460 °C) annealed 1 uc FeSe/STO samples, the large $d_{\text{Fe-Ti}}$ interface was observed more frequently. Transition regions between large and small $d_{\text{Fe-Ti}}$ interface were occasionally observed (Extended Data Fig. 7).

To correlate the interface structure and phonons with superconducting properties, we measured the superconducting gap of the 1 uc FeSe/STO samples with varying annealing temperatures. Because both STEM–EELS and STM–STS are local probes, we performed multiple measurements in the same region with both techniques. Histograms in Fig. 4d show that the mean and largest $\Delta$ both increase with annealing temperature. However, regions without observable gap opening at 5 K were also encountered, which is probably related to the coexistence of large and small $d_{\text{Fe-Ti}}$ interfaces in 1 uc FeSe/STO samples.

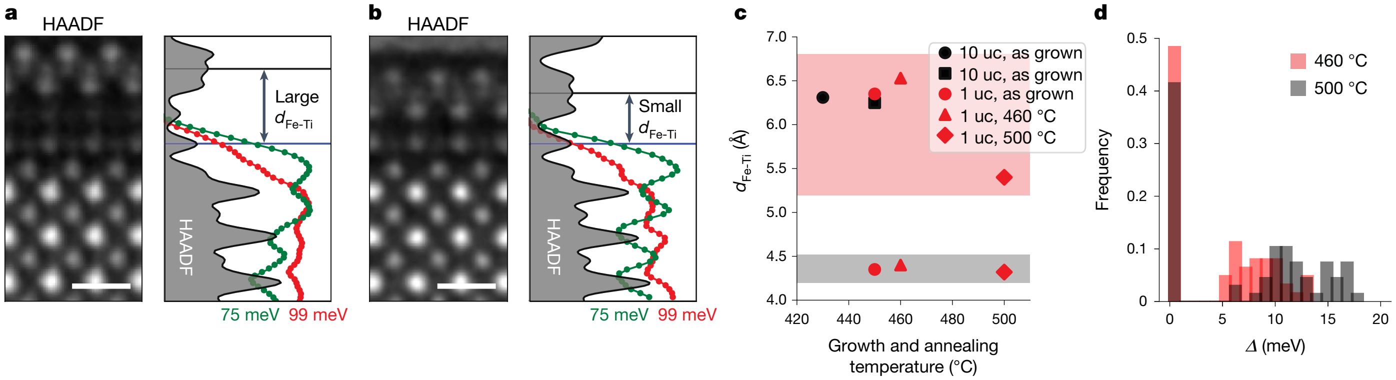

**Fig. 4 | Influence of interlayer spacing on phonons and superconductivity. a**, Left, HAADF–STEM image of FeSe/STO interface with large interlayer spacing, $d_{\text{Fe-Ti}}$. Right, intensity line profiles of 75 and 99 meV phonons across the large $d_{\text{Fe-Ti}}$ interface. **b**, HAADF image and phonon line profiles across the small $d_{\text{Fe-Ti}}$ interface. The Fe layer in FeSe and top-most TiO$_x$ layer are indicated by the two horizontal lines. **c**, $d_{\text{Fe-Ti}}$ measured from various samples with different growth and annealing temperature. **d**, Statistical distribution of superconducting gap measured at 5 K from 1 uc FeSe/STO samples with different annealing temperatures. Scale bars, 5 Å.

## Discussion and conclusion

Our approach demonstrates the ability to understand the phonon modes of a complex interface by resolving the fine distinctions in atomic-scale vibrational characteristics. With the selectivity in **q**-transfer direction, we captured the out-of-plane vibrations of oxygen atoms in both the STO substrate and the interfacial double-$TiO_x$ layer. The presence of the double-$TiO_x$ layer facilitates the out-of-plane vibrations of oxygen in Ti–O layer 1, thereby providing an extra phonon mode for EPC. These out-of-plane vibrations create dipole moments that are essential for coupling with electrons[46]. Besides the high- and low-energy modes discovered here, it is conceivable that other structures of Ti–O layer 0 might also show out-of-plane vibrations closer to the FeSe film[6].

Furthermore, we discovered the coexistence of two types of interface in superconducting 1 uc FeSe/STO samples, characterized by different $d_{\text{Fe-Ti}}$. The correlation between $d_{\text{Fe-Ti}}$ and $\Delta$ indicates that the EPC is rather short ranged, given the variation between large and small $d_{\text{Fe-Ti}}$ is relatively small compared to the spatial extent of the Fuchs–Kliewer phonons. This variation in $d_{\text{Fe-Ti}}$ may account for the broad range of reported $T_c$ and the pseudogap behaviour[38,47–49]. These findings indicate a close relationship between the interface structure and EPC, highlighting the importance of interface homogeneity for the high $T_c$ of 1 uc FeSe/STO.

In conclusion, our vibrational spectroscopy with **q**-selectivity has provided detailed imaging of atomic vibrations at the 1 uc FeSe/STO interface. We identified strong EPC contributions from out-of-plane oxygen vibrations at the interfacial double-$TiO_x$ layer and at the apical oxygens of STO. The observed variation in interlayer spacing correlates with superconducting gap, suggesting the crucial role of spacing in influencing EPC strength and superconductivity. These findings offer microscopic insights into the $T_c$ enhancement at this unique interface and guidance for discovering new high $T_c$ superconductors in which interface effects are critical.

## Online content

Any methods, additional references, Nature Portfolio reporting summaries, source data, extended data, supplementary information, acknowledgements, peer review information; details of author contributions and competing interests; and statements of data and code availability are available at https://doi.org/10.1038/s41586-024-08118-0.

1. Wang, Q. Y. et al. Interface-induced high-temperature superconductivity in single unit-cell FeSe films on $SrTiO_3$. *Chin. Phys. Lett.* **29**, 037402 (2012).
2. Lee, J. J. et al. Interfacial mode coupling as the origin of the enhancement of Tc in FeSe films on $SrTiO_3$. *Nature* **515**, 245–248 (2014).
3. Peng, R. et al. Tuning the band structure and superconductivity in single-layer FeSe by interface engineering. *Nat. Commun.* **5**, 5044 (2014).
4. Liu, X. et al. Dichotomy of the electronic structure and superconductivity between single-layer and double-layer FeSe/$SrTiO_3$ films. *Nat. Commun.* **5**, 5047 (2014).
5. Zhang, C. et al. Ubiquitous strong electron-phonon coupling at the interface of FeSe/$SrTiO_3$. *Nat. Commun.* **8**, 14468 (2017).
6. Shi, R. et al. Atomic-scale observation of localized phonons at FeSe/$SrTiO_3$ interface. *Nat. Commun.* **15**, 3418 (2024).
7. Liu, D. et al. Electronic origin of high-temperature superconductivity in single-layer FeSe superconductor. *Nat. Commun.* **3**, 931 (2012).
8. Zhang, W. et al. Interface charge doping effects on superconductivity of single-unit-cell FeSe films on $SrTiO_3$ substrates. *Phys. Rev. B* **89**, 060506(R) (2014).
9. Zhang, H. et al. Origin of charge transfer and enhanced electron-phonon coupling in single unit-cell FeSe films on $SrTiO_3$. *Nat. Commun.* **8**, 214 (2017).
10. Miyata, Y., Nakayama, K., Sugawara, K., Sato, T. & Takahashi, T. High-temperature superconductivity in potassium-coated multilayer FeSe thin films. *Nat. Mater.* **14**, 775–779 (2015).
11. Lei, B. et al. Evolution of high-temperature superconductivity from a low-Tc phase tuned by carrier concentration in FeSe thin flakes. *Phys. Rev. Lett.* **116**, 077002 (2016).
12. Wen, C. H. P. et al. Anomalous correlation effects and unique phase diagram of electron-doped FeSe revealed by photoemission spectroscopy. *Nat. Commun.* **7**, 10840 (2016).
13. Zhang, W. H. et al. Direct observation of high-temperature superconductivity in one-unit-cell FeSe films. *Chin. Phys. Lett.* **31**, 017401 (2014).
14. Ge, J. F. et al. Superconductivity above 100 K in single-layer FeSe films on doped $SrTiO_3$. *Nat. Mater.* **14**, 285–289 (2015).
15. He, S. et al. Phase diagram and electronic indication of high-temperature superconductivity at 65 K in single-layer FeSe films. *Nat. Mater.* **12**, 605–610 (2013).
16. Tan, S. et al. Interface-induced superconductivity and strain-dependent spin density waves in FeSe/$SrTiO_3$ thin films. *Nat. Mater.* **12**, 634–640 (2013).
17. Xu, Y. et al. Spectroscopic evidence of superconductivity pairing at 83 K in single-layer FeSe/$SrTiO_3$ films. *Nat. Commun.* **12**, 2840 (2021).
18. Fan, Q. et al. Plain s-wave superconductivity in single-layer FeSe on $SrTiO_3$ probed by scanning tunnelling microscopy. *Nat. Phys.* **11**, 946–952 (2015).
19. Song, Q. et al. Evidence of cooperative effect on the enhanced superconducting transition temperature at the FeSe/$SrTiO_3$ interface. *Nat. Commun.* **10**, 758 (2019).
20. Liu, C. et al. High-order replica bands in monolayer FeSe/$SrTiO_3$ revealed by polarization-dependent photoemission spectroscopy. *Nat. Commun.* **12**, 4573 (2021).
21. Faeth, B. D. et al. Interfacial electron-phonon coupling constants extracted from intrinsic replica bands in monolayer FeSe/$SrTiO_3$. *Phys. Rev. Lett.* **127**, 016803 (2021).
22. Fuchs, R. & Kliewer, K. L. Optical modes of vibration in an ionic crystal slab. *Phys. Rev.* **140**, A2076 (1965).
23. Zhang, S. et al. Role of $SrTiO_3$ phonon penetrating into thin FeSe films in the enhancement of superconductivity. *Phys. Rev. B* **94**, (2016).
24. Zhang, S. et al. Enhanced superconducting state in FeSe/$SrTiO_3$ by a dynamic interfacial polaron mechanism. *Phys. Rev. Lett.* **122**, 066802 (2019).
25. Li, F. et al. Atomically resolved FeSe/$SrTiO_3$(001) interface structure by scanning transmission electron microscopy. *2D Mater.* **3**, 024002 (2016).
26. Sims, H. et al. Intrinsic interfacial van der Waals monolayers and their effect on the high-temperature superconductor FeSe/$SrTiO_3$. *Phys. Rev. B* **100**, 144103 (2019).
27. Peng, R. et al. Picoscale structural insight into superconductivity of monolayer FeSe/$SrTiO_3$. *Sci. Adv.* **6**, eaay4517 (2020).
28. Krivanek, O. L. et al. Vibrational spectroscopy in the electron microscope. *Nature* **514**, 209–212 (2014).
29. Venkatraman, K., Levin, B. D. A., March, K., Rez, P. & Crozier, P. A. Vibrational spectroscopy at atomic resolution with electron impact scattering. *Nat. Phys.* **15**, 1237–1241 (2019).
30. Hage, F. S., Radtke, G., Kepaptsoglou, D. M., Lazzeri, M. & Ramasse, Q. M. Single-atom vibrational spectroscopy in the scanning transmission electron microscope. *Science* **367**, 1124–1127 (2020).
31. Xu, M. et al. Single-atom vibrational spectroscopy with chemical-bonding sensitivity. *Nat. Mater.* **22**, 612–618 (2023).
32. Yan, X. et al. Single-defect phonons imaged by electron microscopy. *Nature* **589**, 65–69 (2021).
33. Yan, X. et al. Real-space visualization of frequency-dependent anisotropy of atomic vibrations. Preprint at https://arxiv.org/abs/2312.01694 (2023).
34. Erdman, N. et al. The structure and chemistry of the $TiO_2$-rich surface of $SrTiO_3$ (001). *Nature* **419**, 55–58 (2002).
35. Kubo, T. & Nozoye, H. Surface structure of $SrTiO_3$(100). *Surf. Sci.* **542**, 177–191 (2003).
36. Andersen, T. K., Fong, D. D. & Marks, L. D. Pauling's rules for oxide surfaces. *Surf. Sci. Rep.* **73**, 213–232 (2018).
37. Zou, K. et al. Role of double $TiO_2$ layers at the interface of FeSe/$SrTiO_3$ superconductors. *Phys. Rev. B* **93**, 180506 (2016).
38. Pedersen, A. K. et al. Interfacial superconductivity in FeSe ultrathin films on $SrTiO_3$ probed by in situ independently driven four-point-probe measurements. *Phys. Rev. Lett.* **124**, 227002 (2020).
39. Hage, F. S., Kepaptsoglou, D. M., Ramasse, Q. M. & Allen, L. J. Phonon spectroscopy at atomic resolution. *Phys. Rev. Lett.* **122**, 016103 (2019).
40. Yang, H. et al. Inelastic electron scattering at large angles: the phonon polariton contribution. Preprint at https://arxiv.org/abs/2401.04719 (2024).
41. Nicholls, R. J. et al. Theory of momentum-resolved phonon spectroscopy in the electron microscope. *Phys. Rev. B* **99**, 094105 (2019).
42. Zeiger, P. M. & Rusz, J. Efficient and versatile model for vibrational STEM-EELS. *Phys. Rev. Lett.* **124**, 025501 (2020).
43. Rademaker, L., Wang, Y., Berlijn, T. & Johnston, S. Enhanced superconductivity due to forward scattering in FeSe thin films on $SrTiO_3$ substrates. *New J. Phys.* **18**, 022001 (2016).
44. Rademaker, L., Alvarez-Suchini, G., Nakatsukasa, K., Wang, Y. & Johnston, S. Enhanced superconductivity in FeSe/$SrTiO_3$ from the combination of forward scattering phonons and spin fluctuations. *Phys. Rev. B* **103**, 144504 (2021).
45. Zhao, W. et al. Direct imaging of electron transfer and its influence on superconducting pairing at FeSe/$SrTiO_3$ interface. *Sci. Adv.* **4**, eaao2682 (2018).
46. Lee, D. H. What makes the Tc of FeSe/$SrTiO_3$ so high? *Chin. Phys. B* **24**, 117405 (2015).
47. Kang, B. L. et al. Preformed Cooper pairs in layered FeSe-based superconductors. *Phys. Rev. Lett.* **125**, 97003 (2020).
48. Faeth, B. D. et al. Incoherent Cooper pairing and pseudogap behavior in single-layer FeSe/$SrTiO_3$. *Phys. Rev. X* **11**, 021054 (2021).
49. Ide, K., Tanaka, T., Pedersen, A., Ichinokura, S. & Hirahara, T. Temperature dependence of the superconducting gap of single-layer FeSe/$SrTiO_3$: direct comparison between transport and spectroscopic measurements. *Phys. Rev. Mater.* **6**, 124801 (2022).

# Methods

### FeSe/STO thin film growth and STM–STS measurements

The FeSe films with varying thickness (1, 3, 10 uc) were grown on Nb-doped (0.5% wt) STO (001) substrates by the reported method[1]. The as-grown 1 uc FeSe/STO samples were characterized by in situ STM at room temperature. Then, the 1uc FeSe/STO samples were capped with amorphous Se layers more than 10 nm thick and transferred to the Unisoku UHV low-temperature scanning tunnelling microscope-molecular beam epitaxial system for STM–STS measurements. Before the STM and STS measurements, postannealing in UHV was conducted to remove the Se capping layers and to make the 1 uc samples superconducting[50]. The postannealing parameters were: $\Delta$ roughly 15 mV sample (500 °C for 2 h) and $\Delta$ roughly 10 mV sample (460 °C for 6 h). Polycrystalline Pt–Ir tips, cleaned by electron beam bombardment and verified on Au (111), were used in the STM–STS measurements. The STM topographic images were acquired in constant-current mode with the bias voltage applied to the sample. Unless otherwise specified, the STM experiments were performed at 5.0 K and the STS were measured with a bias modulation of 0.5 mV at 1,517 Hz.

### TEM sample preparation

TEM specimens of FeSe/STO were prepared using a Tescan dual beam SEM–FIB. Before the SEM–FIB experiments, we deposited a 500–1,000 nm amorphous carbon protection layer above the Te capping film. The cross-section TEM specimens were prepared by a standard lift-out procedure from the same 100 × 100 μm region in which STM–STS measurements were performed. The final polishing was done with 3–5 kV Ga ion beam followed by 700–900 eV Ar ion beam polishing using a Fischione 1040 Nanomill. Before STEM–EELS experiments, the TEM specimens were cleaned in the TEM sample holder by a mild bake under UHV at 80–120 °C.

### STEM imaging

HAADF–STEM imaging was performed using both JEOL JEM-ARM300F transmission electron microscope at 300 kV and Nion UltraSTEM HERMES200 at 60 kV. The FeSe/STO interface, in particular the 1 uc FeSe film, is prone to electron beam damage, which can be mitigated by low dose and low acceleration voltage. We used a low-dose condition (5 pA beam current) for high-resolution HAADF–STEM imaging to avoid damaging the 1 uc FeSe film on STO. The convergence half angle was 30 mrad. HAADF collection angle was 80–180 mrad. HAADF images in Figs. 1 and 4 are results of aligned and summed 10–12 frames of HAADF images acquired with 1 μs per pixel dwell time.

### Monochromated EELS

EELS experiments were conducted at 60 kV using a Nion UltraSTEM HERMES200. The microscope was equipped with a source monochromator and the Dectris ELA direct electron detector for EELS acquisition. The beam convergence and EELS collection half angles in our experiments were 33 and 17 mrad, respectively. The energy resolution of on-axis EELS was about 7 meV, as measured from the full-width at half-maximum of the zero-loss peak (ZLP). In the dark-field EELS condition, we displaced the whole diffraction pattern using diffraction dipoles in the projector lens such that the electrons scattered outside of the bright-field disk were collected through the EELS entrance aperture. The angle of diffraction tilt we typically used was between 70 and 85 mrad. We corrected the extra EELS aberrations at large angles due to the diffraction tilt up to the second order. Under this condition, the energy resolution of dark-field EELS was about 9 meV, as measured from the ZLP full-width at half-maximum when the beam passed through a thin amorphous carbon film. We adjusted the monochromator slit size such that the monochromated ZLP contained 3–5% of the total beam current, which is typically 4 to 5 pA. The small beam current also helped to mitigate the beam damage to the 1 uc FeSe film. For dark-field vibrational EELS, we used 0.5 meV per channel for the EELS dispersion, 0.35 Å/pixel size for real-space sampling and 20 to 40 ms for EELS detector exposure time. The typical field of view was about 4 × 4 nm, which gave a total acquisition time for each dataset of 3–4 min. With these parameters, we acquired multiple EELS mapping datasets across the FeSe/STO interface.

For EELS data processing and analysis, we first performed a drift correction on the acquired EELS maps. The short acquisition time resulted in relatively small and linear drift but also resulted in weaker signals, especially for high-energy phonons. To enhance the statistics of the phonon spectral images, we averaged several drift-corrected EELS datasets (Extended Data Fig. 8). Gaussian filtering was applied to further reduce noise. Up to 15 drift-corrected datasets were aligned and summed for each series of out-of-plane and in-plane dark-field-EELS energy-filtered maps shown in Fig. 2. The layer and column-resolved EEL spectra were extracted from the summed EELS datasets. The layer resolved dark-field vibrational EELS in Fig. 1 shows the results of summed spectra from out-of-plane and in-plane acquisitions. Background subtraction for vibrational EEL spectra in Figs. 1 and 2 was performed using a previously reported Pearson VII function[51,52]. We also multiplied the background subtracted EELS with energy $E$ to take into account the Boson occupation statistics at finite temperature[53]. For phonon spectral maps, we simply removed the background by using the $I(E) \times E^p$ method[52] to avoid introducing artefacts from background fitting, where $I(E)$ is the raw EELS intensity, $E$ is energy of the EELS spectrum and $p$ is the exponent of $E$. No normalization of EEL spectra was done when producing the phonon spectral images. Therefore, the images can be thought of as energy-filtered annular dark-field images with asymmetric detector placement. All EELS data analysis was done using our custom Python code.

### DFT calculations

The calculations for FeSe/TiO$_x$/STO were performed using DFT with the projector-augmented wave pseudopotentials[54,55] and the local density approximation[56] using Vienna Ab initio Simulation Package[57] code. An energy cut-off of 550 eV and a 4 × 4 × 1 Monkhorst–Pack **k**-point grid was used[58]. The calculations of phonon bands were based on density-functional perturbation theory (DFPT)[59–61]. The structure was optimized until the atomic forces were smaller than 0.001 eV/Å. The vacuum layer was 15 Å thick to ensure decoupling between neighbouring slabs. The Hubbard $U$ term[62] with $U = 3.2$ and $J = 0.9$ eV was considered for the Ti-3$d$ orbitals.

The superconducting properties were calculated by QUANTUM ESPRESSO code[63] using the Perdew–Burke–Ernzerhof[64] ultrasoft pseudopotentials. A cut-off of 60 Ry was used for the wave functions and 600 Ry for the charge densities. The Brillouin zone sampling used 16 × 16 × 1 Monkhorst–Pack **k**-point grids. Using the above **k** point samplings for the self-consistent cycle, the dynamic matrices were calculated on a 4 × 4 × 1 **q**-point mesh and a broadening $\eta = 0.015$ Ry was used. The lattice constants were set to the experimental values of bulk STO, with a lattice parameter $a = 3.905$ Å (ref. 65).

### FRFPMS simulations

FRFPMS[66] were performed using a set of snapshots generated using phonon eigenmodes calculated by DFT. A supercell of size 3.86 × 3.50 × 25.49 nm was generated, following the maximal sample thickness used in experiments. This supercell consisted of 5 and 33 repetitions of the DFT FeSe/Ti$_2$O$_2$/STO simulation cell along the supercell $a$ and $c$ axes, respectively. Phonon eigenmodes were evaluated on a grid of 5 × 1 × 33 **q**-points, to guarantee periodicity of atomic displacements across the supercell boundaries. Convergence and collection angles and aperture positions were set according to experiments. To generate atomic displacements, the DFT-calculated phonon modes were first distributed into 26 frequency bins based on their eigenfrequencies (ignoring the modes with imaginary frequencies) starting from 0 up to 26 THz, with a bin width of 1 THz. Then we followed a procedure outlined in ref. 67 separately for every energy bin, to generate 200 snapshots in each frequency bin. Multislice simulations were performed using DrProbe[68]. STEM simulation was calculated on a grid of 32 × 92 beam positions spanning the region of 7.72 × 22.2 Å with a scan step of roughly 0.24 Å along both dimensions.

## Data availability

Raw data for key experimental results are presented in Extended Data Figs. 3 and 8. Further data can be requested from the corresponding author.

50. Guan, J. et al. Superconducting transition of FeSe/SrTiO$_3$ induced by adsorption of semiconducting organic molecules. *Phys. Rev. B* **95**, 205405 (2017).
51. Qi, R. et al. Four-dimensional vibrational spectroscopy for nanoscale mapping of phonon dispersion in BN nanotubes. *Nat. Commun.* **12**, 1179 (2021).
52. Hoglund, E. R. et al. Emergent interface vibrational structure of oxide superlattices. *Nature* **601**, 556–561 (2022).
53. Batson, P. E. & Lagos, M. J. Interpretation of meV resolution phonon EELS data. *Microsc. Microanal.* **24**, 412–413 (2018).
54. Blochl, P. E. Projector augmented-+rave method. *Phys. Rev. B* **50**, 24 (1994).
55. Kresse, G. & Joubert, D. From ultrasoft pseudopotentials to the projector augmented-wave method. *Phys. Rev. B* **59**, 1758–1775 (1999).
56. Perdew, J. P. & Zunger, A. Self-interaction correction to density-functional approximations for many-electron systems. *Phys. Rev. B* **23**, 5048–5079 (1981).
57. Kresse, G. & Furthmüller, J. Efficient iterative schemes for ab initio total-energy calculations using a plane-wave basis set. *Phys. Rev. B* **54**, 11169–11186 (1996).
58. Methfessel, M. & Paxton, A. T. High-precision sampling for Brillouin-zone integration in metals. *Phys. Rev. B* **40**, 3616–3621 (1989).
59. Baroni, S., De Gironcoli, S., Corso, A. D. & Giannozzi, P. Phonons and related crystal properties from density-functional perturbation theory. *Rev. Mod. Phys.* **73**, 515–562 (2001).
60. Gonze, X. First-principles responses of solids to atomic displacements and homogeneous electric fields: Implementation of a conjugate-gradient algorithm. *Phys. Rev. B* **55**, 10337–10354 (1997).
61. Gonze, X. & Lee, C. Dynamical matrices, Born effective charges, dielectric permittivity tensors, and interatomic force constants from density-functional perturbation theory. *Phys. Rev. B* **55**, 10355–10368 (1997).
62. Anisimov, V. I., Zaanen, J. & Andersen, O. K. Band theory and Mott insulators: Hubbard U instead of Stoner I. *Phys. Rev. B* **44**, 943–954 (1991).
63. Giannozzi, P. et al. QUANTUM ESPRESSO: a modular and open-source software project for quantum simulations of materials. *J. Phys. Condens. Matter* **21**, 395502 (2009).
64. Perdew, J. P., Burke, K. & Ernzerhof, M. Generalized gradient approximation made simple. *Phys. Rev. Lett.* **77**, 3865–3868 (1996).
65. Mitchell, R. H., Chakhmouradian, A. R. & Woodward, P. M. Crystal chemistry of perovskite-type compounds in the tausonite-loparite series, (Sr$_{1-2x}$Na$_x$La$_x$)TiO$_3$. *Phys. Chem. Miner.* **27**, 583–589 (2000).
66. Zeiger, P. M. & Rusz, J. Frequency-resolved frozen phonon multislice method and its application to vibrational electron energy loss spectroscopy using parallel illumination. *Phys. Rev. B* **104**, 104301 (2021).
67. Chen, X., Kim, D. S. & LeBeau, J. M. A comparison of molecular dynamics potentials used to account for thermal diffuse scattering in multislice simulations. *Ultramicroscopy* **244**, 113644 (2023).
68. Barthel, J. Dr. Probe: a software for high-resolution STEM image simulation. *Ultramicroscopy* **193**, 1–11 (2018).

**Acknowledgements** This work was primarily supported by the US Department of Energy (DOE), Office of Basic Energy Sciences, Division of Materials Sciences and Engineering, under Award No. DE-SC0014430 (H.Y. and X.P.). Further support was provided by the DOE's National Nuclear Security Administration under grant no. GRANT13583770 (F.G. and X.P.) and the National Science Foundation through the Materials Research Science and Engineering Center programme under grant award no. DMR-2011967 (X.Y. and X.P.). Y.Z. and R.W. were supported by the US DOE, Office of Science (grant no. DE-FG02-05ER46237). P.Z. and J.R. acknowledge the support of the Swedish Research Council (grant no. 2021-03848), Olle Engkvist's foundation (grant no. 214-0331), STINT (grant no. CH2019-8211) and Knut and Alice Wallenbergs' foundation (grant no. 2022.0079). The electron microscopy studies were performed at the UC Irvine Materials Research Institute (IMRI) supported in part by the National Science Foundation through the Materials Research Science and Engineering Center programme (grant no. DMR-2011967). The simulations were enabled by resources provided by the National Academic Infrastructure for Supercomputing in Sweden (NAISS) at NSC Centre partially funded by the Swedish Research Council through grant agreement no. 2022-06725. H.Y. acknowledges L.D. Marks for valuable discussions on the surface structure of SrTiO$_3$. H.Y. also thanks M. Xu for assistance with low-dose STEM imaging, as well as W. Wang and H. Wu for helping with TEM specimen preparation.

**Author contributions** X.P. conceived and directed this project. H.Y. proposed and designed the research with input from J.G., R.W. and X.P. H.Y. carried out TEM specimen preparation, STEM–EELS experiments and data analysis. Y.Z. and R.W. designed and performed DFT simulations. G.M. and Xiaofeng Xu grew FeSe/STO samples with supervision from X.Z. and J.G. G.M. performed STM–STS experiments with supervision from W.W. and J.G. J.R. did FRFPMS simulations with input from P.Z. and Y.Z. F.G. and H.Y. performed STEM image simulations. Xianghan Xu grew the FeSe bulk single crystal. X.Y. and T.A. helped with STEM–EELS experiments. The manuscript was prepared by H.Y., Y.Z., R.W. and X.P., with contributions from all other co-authors.

**Competing interests** The authors declare no completing interests.

**Additional information**
**Supplementary information** The online version contains supplementary material available at https://doi.org/10.1038/s41586-024-08118-0.
**Correspondence and requests for materials** should be addressed to Xiaoqing Pan.
**Peer review information** *Nature* thanks Louk Rademaker and the other, anonymous, reviewer(s) for their contribution to the peer review of this work. Peer reviewer reports are available.

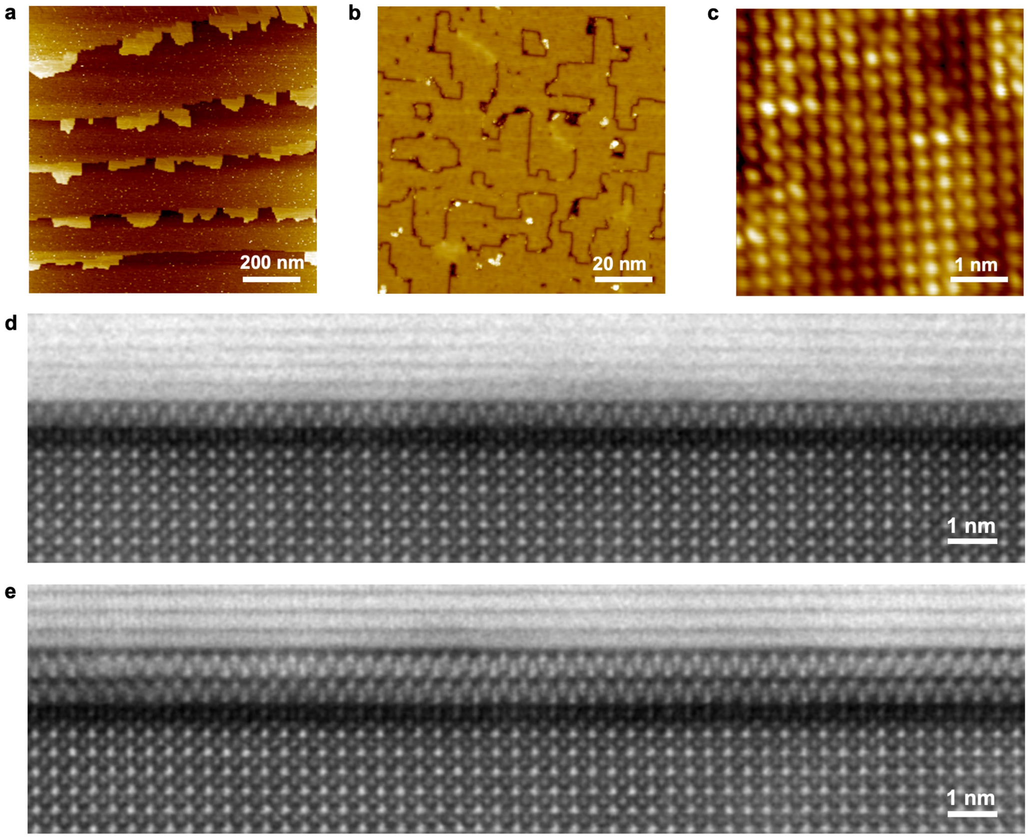

**Extended Data Fig. 1 | STM and STEM images of the 1uc FeSe/STO samples.** (a) A large-scale STM image of the 1uc FeSe film on STO before post-annealing and Te capping, with some brighter islands due to 2uc FeSe at the edges of the STO surface steps. (b) and (c) zoom-in STM image after post-annealing. (d) Low-magnification cross-section HAADF image of the same sample after Te capping, showing a typical 1uc FeSe region. (e) HAADF image of a 2uc FeSe region from the same 1uc FeSe/STO sample.

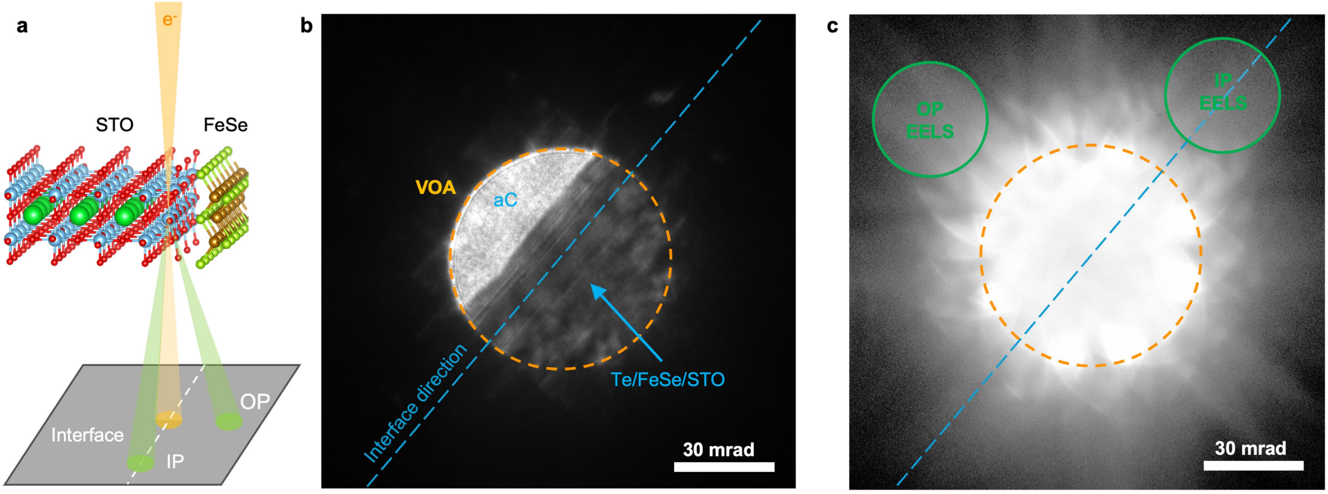

**Extended Data Fig. 2 | Schematic of the momentum-selective dark-field EELS experiment.** (a) Scattering geometry (b) A diffraction pattern under defocused condition showing a shadow image of the TEM specimen of amorphous carbon/Te/FeSe/STO and the interface direction. (c) A diffraction pattern with intensity shown in log scale. The electron beam focused on the STO region. The EELS entrance aperture locations for OP and IP acquisitions are shown in (b).

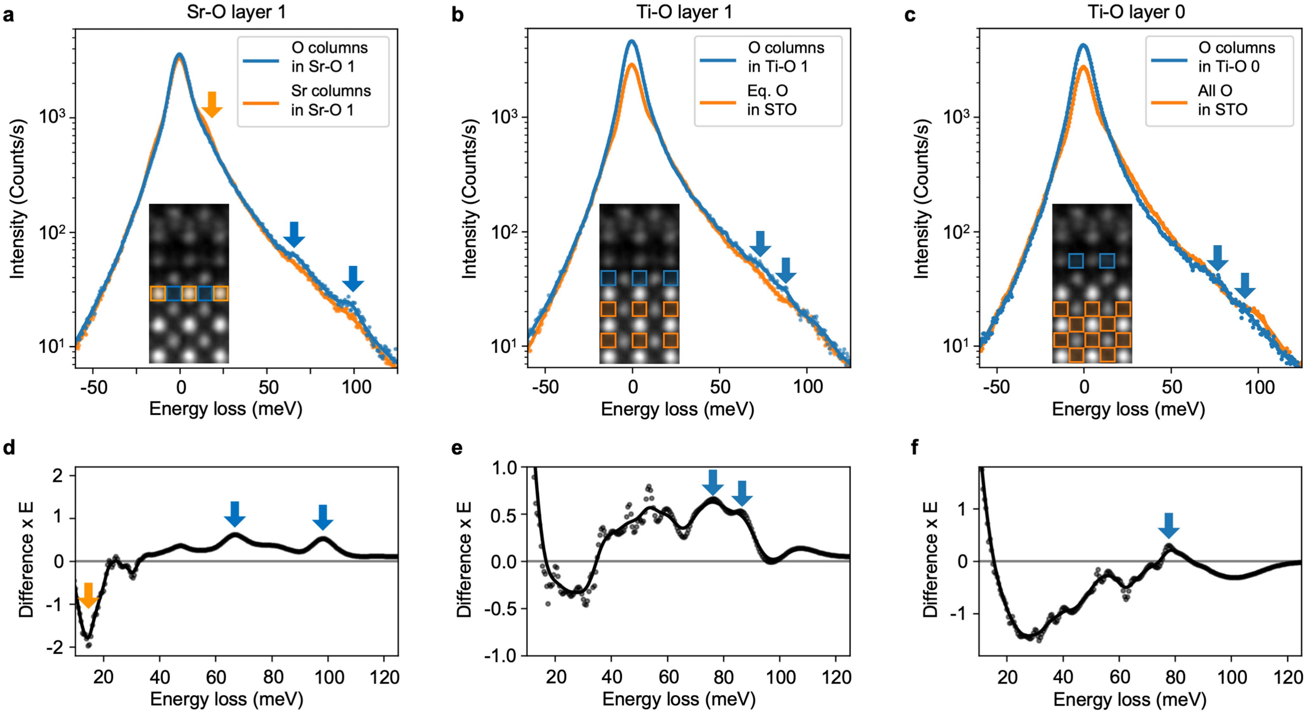

**Extended Data Fig. 3 | Raw columns resolved dark-field EELS.** (a) EELS of O and Sr columns in the Sr-O layer 1. The 14 meV peak corresponds to the Sr phonons, 65 and 100 meV phonon peaks are stronger on the O column. (b) O columns in the Ti-O layer 1 (blue curve) compared with equatorial O columns in STO (orange curve). New vibrational loss peaks near 76 and 85 meV are indicated by the blue arrows, which are associated with the Ti-O bonding between Ti-O layer 1 and 0. (c) O columns in the Ti-O layer 0 (blue curve) compared with the average of both apical and equatorial O columns in STO (orange curve). All EEL spectra in (d, e, f) are from OP measurements. The EELS acquisition locations are shown with color-matching rectangles in the inserted HAADF image (dimension 1 × 2 nm). Differences between each pair of EEL spectra in (a, b, c) are plotted in (d, e, f). The spectra are multiplied with E to better visualized the EELS intensity differences as a function of energy.

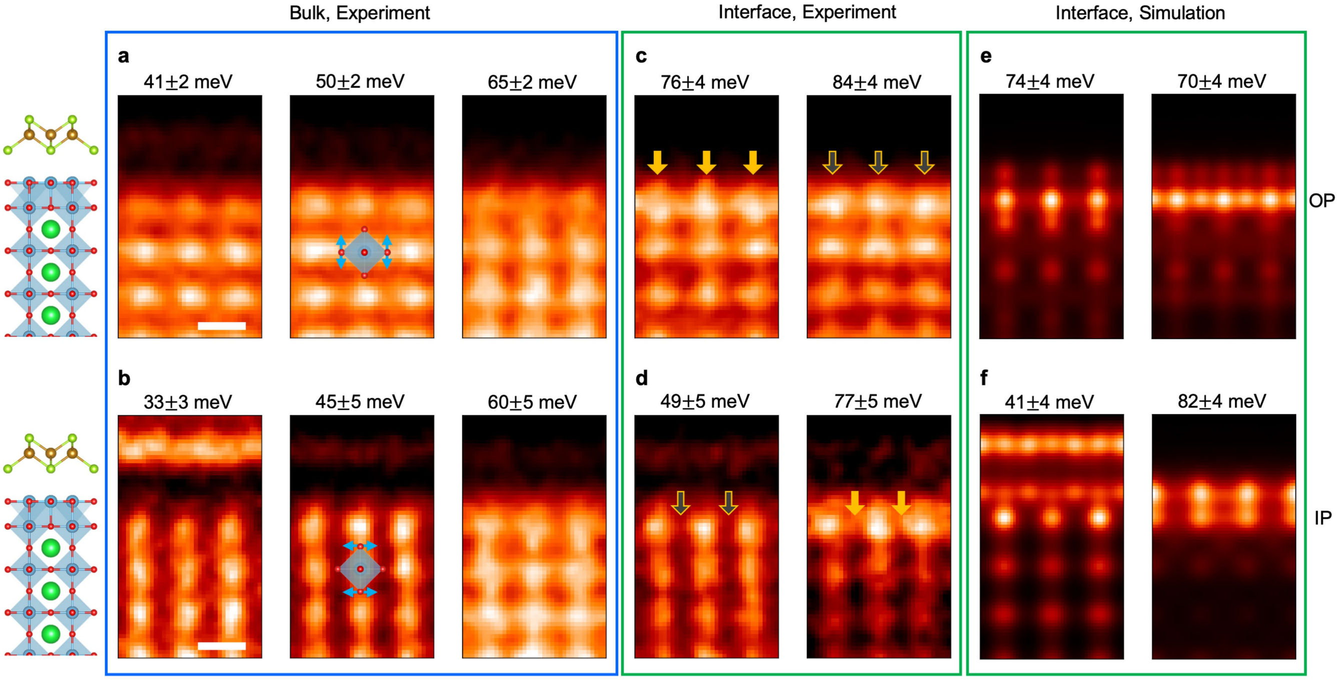

**Extended Data Fig. 4 | Additional phonon spectral images.** (a, b) Medium energy Ti+O phonon maps from OP and IP acquisition, respectively. The bright atomic columns in the STO region correspond to the Ti + O atom columns. The images show elongation in either horizontal (41 meV and 50 meV, OP) or vertical (33 meV and 45 meV, IP) direction. This is due to the vibration of different O columns near the Ti + O columns, as illustrated with the $TiO_6$ octahedrons in the 50 meV OP and 45 meV IP images. The oxygen vibration directions are indicated with double headed arrows. The 60 meV and 65 meV images involve all O columns surrounding the Ti + O columns, therefore show less elongations. (c, d) OP and IP interface phonons. The OP interface phonons were found between 76 and 84 meV, whereas the IP interface vibrations were observed near 50 meV and 77 meV. The vibration of the "O" columns in Ti-O layer 0 is stronger at 76 meV than at 84 meV in the OP maps, as indicated by the solid and open arrows. The two IP interface phonon maps differ from each other by their vibrational intensity of O in Ti-O layer 1. The stronger oxygen column vibrations were observed in the 77 meV map, as indicated by the arrows as well. (e, f) FRFPMS simulation of the interface phonons correspond to (c, d), which agree qualitatively with EELS data.

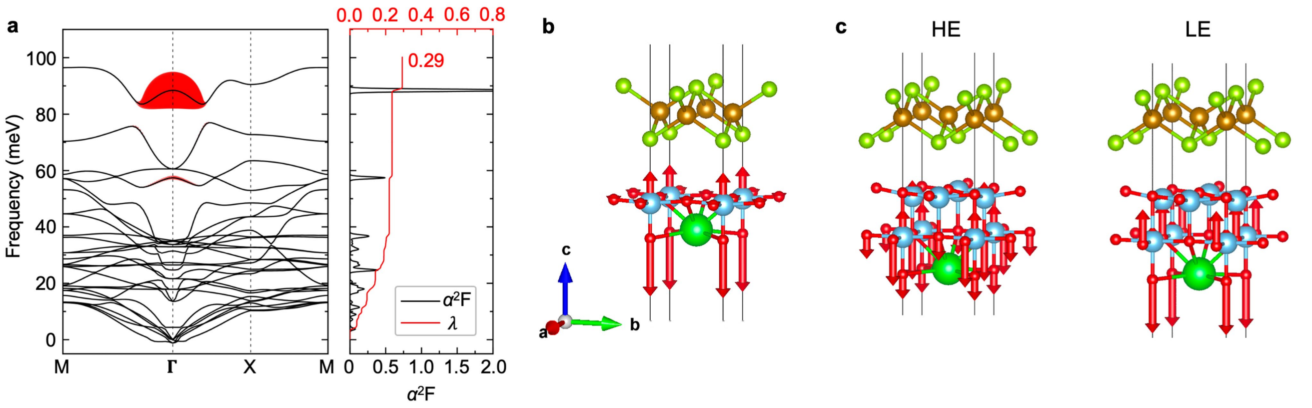

**Extended Data Fig. 5 | Electron-phonon coupling of 1uc STO models.** (a) The phonon dispersions for the structure FeSe/STO (1uc, without additional $TiO_x$ layer) with phonon linewidth $\gamma_{qv}$ denoted by red circles. The right panel shows the Eliashberg spectral function $\alpha^2F(\omega)$ (black line) and cumulative frequency-dependent $\lambda(\omega)$ (red line). (b) The atomic displacements for the 88 meV strong-coupling modes in (a) at $\mathbf{q} = 0$. (c) The atomic displacements for the HE and LE modes at 78.0 and 65.7 meV, calculated for the FeSe/$Ti_2O_2$/STO (1uc) model in Fig. 3. The additional $Ti_2O_2$ interfacial layer introduces new out-of-plane vibration modes of O atoms in Ti-O layer 1.

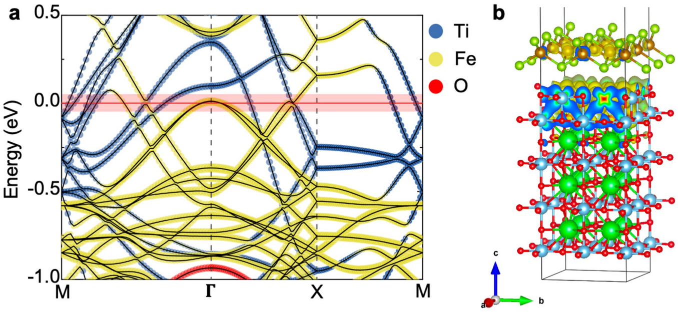

**Extended Data Fig. 6 | Electronic structure of FeSe/$Ti_2O_2$/STO.** (a) The band structures and projected orbital contributions. The blue, yellow, and red dots represent the total orbital contributions of Ti, Fe, and O, respectively. The red shaded area in [−0.05, 0.05] eV corresponds to the energy range for the charge density plot in (b). (b) The charge density (yellow) with electronic states around the Fermi level with the isosurface values of 0.0005 e/bohr$^3$.

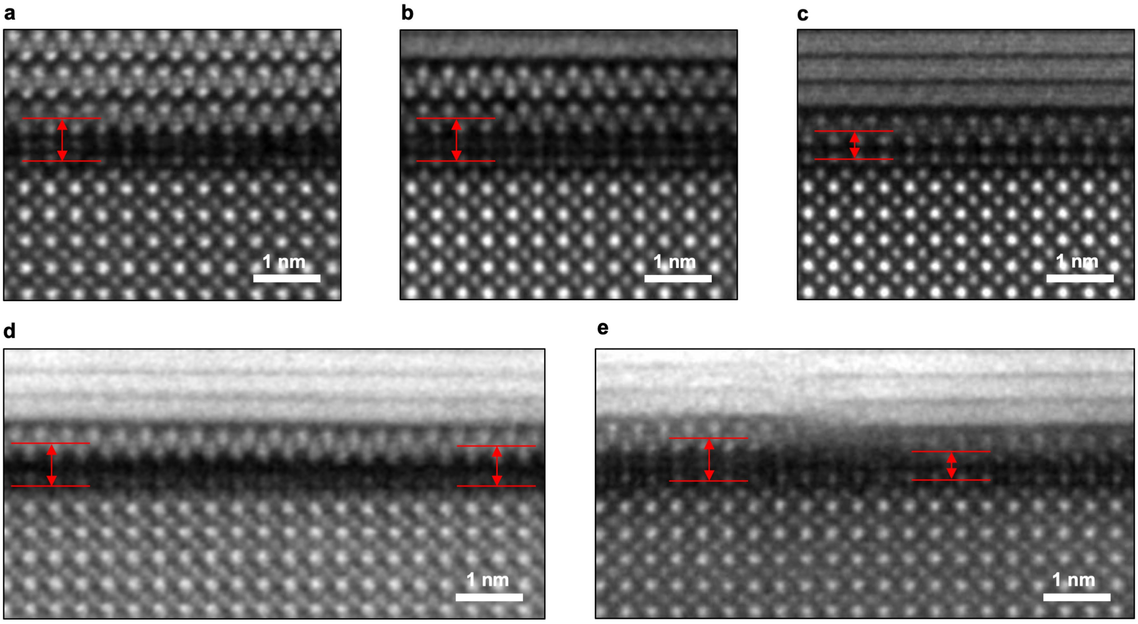

**Extended Data Fig. 7 | HAADF-STEM images of FeSe/STO interfaces with different $d_{\text{Fe-Ti}}$.** (a) An as-grown 10uc FeSe/STO sample with large $d_{\text{Fe-Ti}}$ interface. (b) A 2uc FeSe region in the 500 °C annealed sample with large $d_{\text{Fe-Ti}}$. (c) A different region from the same specimen in (b) but with small $d_{\text{Fe-Ti}}$. (d) A region in the 500 °C annealed sample featuring gradual interface structure transition from large $d_{\text{Fe-Ti}}$ (left) to small $d_{\text{Fe-Ti}}$ (right). (e) A region in the 460 °C annealed sample featuring sharp interface structure transition from large $d_{\text{Fe-Ti}}$ to small $d_{\text{Fe-Ti}}$. The transition region has disorders in the FeSe film. The vertical positions of the Fe layer in the 1uc FeSe and the Ti-O layer 0 of STO surface, as well as the corresponding $d_{\text{Fe-Ti}}$ are horizontal lines and double headed arrows.

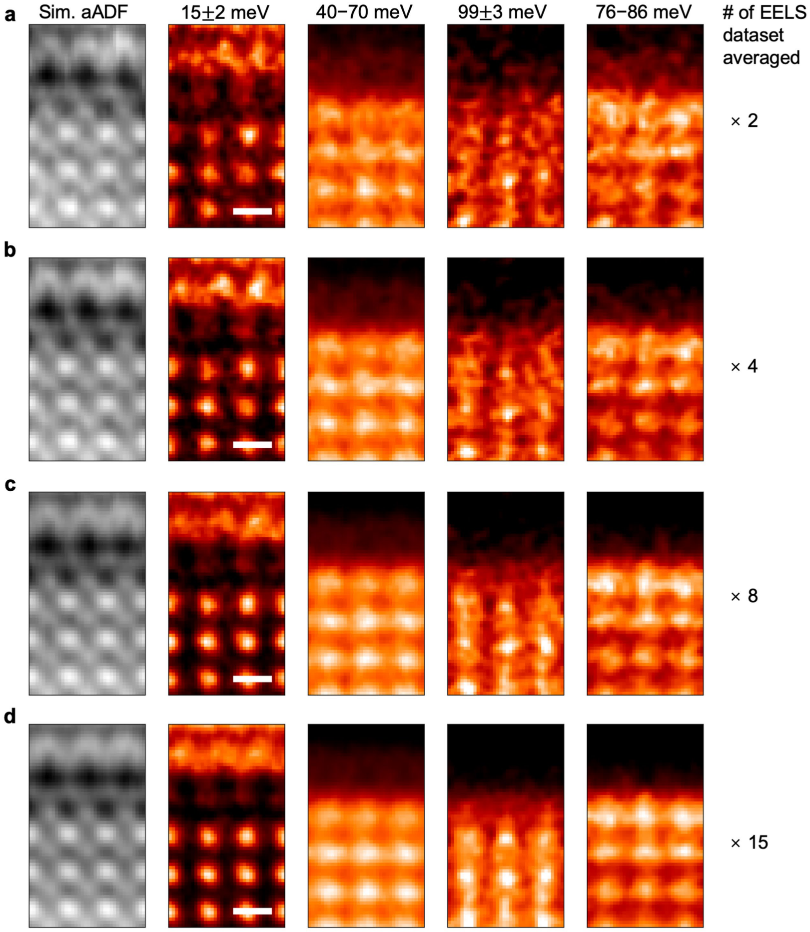

**Extended Data Fig. 8 | Data acquisition and statistical improvement for momentum-selective dark-field EELS mapping.** From left to right: asymmetric annular dark-field (aADF) image acquired simultaneously with EELS mapping, and energy filtered dark-field EELS maps at 15 meV, 40–70, meV 99 meV, 74–86 meV. From top to bottom: sets of images with increasing number of averaged datasets, with (a), (b), (c), and (d) averaging 2, 4, 8, and 15 datasets, respectively.